Understanding keyhole induced-porosities in laser powder bed fusion of aluminum and elimination strategy

Liping Guo[1,2], Hongze Wang[1,2,3,], Hanjie Liu[1,2], Yuze Huang[4], Qianglong Wei[1,2], Chu Lun Alex Leung[5,6], Yi Wu[1,2,3,*], Haowei Wang[1,2,3]*

1 State Key Laboratory of Metal Matrix Composites, Shanghai Jiao Tong University, Shanghai, 200240, China

2 School of Materials Science & Engineering, Shanghai Jiao Tong University, Shanghai, 200240, China

3 Institute of Alumics Materials, Shanghai Jiao Tong University (Anhui), Huaibei, 235000, China

4 Institute for Advanced Manufacturing and Engineering, Coventry University, CV6 5LZ, UK

5 Department of Mechanical Engineering, University College London, London WC1E 7JE, UK

6 Research Complex at Harwell, Harwell Campus, Oxfordshire OX11 0FA, UK

*Email: Hongze Wang, hz.wang@sjtu.edu.cn; Yi Wu, eagle51@sjtu.edu.cn

Abstract

Laser powder bed fusion (LPBF) technology has the potential to revolutionize the fabrication of complex metal components in the aerospace, medical, and automotive industries. However, keyhole pores may be induced during the rapid laser-metal interaction (~10^{-5} s) of the LPBF. These inner porosities can potentially affect the mechanical properties of the fabricated parts. Here, based on the experimentally observed keyhole-penetration pore (KP-pore) led by the keyhole splitting of the molten pool in LPBF, a multi-physics finite volume model was established to reveal this mechanism, where keyhole pores were formed in a gas–solid interaction that is different from the previously reported gas–liquid interaction. The formation mechanisms of the KP-pore, rear-front pore (RF-pore), and rear pore (R-pore) could be attributed to different keyhole fluctuation modes. The effects of the powder on the characteristics of the keyhole, molten pool, and pore formation were explored. The increased pore counts and decreased size were owing to the powder-promoting keyhole and molten pool oscillation. In addition, a relationship map between the input energy density and pore number was built via a high-throughput simulation, providing a strategy to reduce or remove the pores in laser powder bed fusion.

Keywords: laser powder fusion, simulation, keyhole pore, mechanism

Nomenclature		T_b:	boiling point
$\vec{v}$:	Velocity vector	l_h:	Characteristic length for heat conduction
ρ:	Density	L_v:	latent heat of vaporization
t:	Time	P_r:	recoil pressure
p:	Pressure	β_R:	Recondensation coefficient
μ:	Dynamic viscosity	P_{atm}:	Ambient pressure
F_d:	Drag force coefficient	R:	Gas constant
$\vec{G}$:	Body acceleration	P_s:	Surface pressure
h:	Enthalpy	$TSDRG$:	Solidification drag coefficient
k:	Thermal conductivity	λ_1:	Characteristic length of mush zone
T:	Temperature	$\vec{n}$:	Surface normal vector
T_s:	Solidus temperature	h_c:	Heat transfer coefficient
T_l:	liquidus temperature	T_a:	Reference temperature
ρ_s:	Solid density	ρ_l:	Liquid density
C_s:	Specific heat of the solid state	C_l:	Specific heat of the liquid state

h_{sl}:	Fusion enthalpy	σ:	Stefan-Boltzmann constant
F:	Volume of the fluid	ε:	Radiation emissivity
q:	laser heat flux	$\vec{v}_n$:	Normal velocity vector
P:	Laser power	γ:	Surface tension
δ:	Vaporization rate	R_k:	Radius of curvature
A_{sur}:	Effective surface area	r:	Laser spot radius
x, y	Coordinates	d:	Laser spot diameter
V:	Scanning speed		

1. Introduction

Laser powder bed fusion (LPBF) technology, which involves fabricating parts layer by layer *via* a focused laser beam to fuse the loose powder along a pre-designed path, is promising in aerospace, automotive, and medical applications because it is customized and free of geometric limitations that cannot be realized using traditional technologies[1-4]. Nevertheless, concerns over part quality and consistency limit its further application [5, 6]. The variability of the mechanical properties of the LPBF components is due to the unusual thermal history and defects generated during the rapid heating and cooling process in the laser-matter interaction [7-10]. The common defect is porosity, which can be classified into gas pores, lack-of-fusion voids, and keyhole pores [11]. Owing to their different formation mechanisms, they usually exhibit diverse physical characteristics and sizes. Gas pores are relatively small, and most are formed by gas entrapment during the gas atomization or at the end of the building [12]. The influence of these small pores can be ignored. The lack-of-fusion defects are irregular and elongated, generated from the insufficient fusion between the two layers or tracks. This is detrimental, as the sharp crevices and unfused powder can exist in the defect, acting as initial cracks. The lack-of-fusion defects can be eliminated by adjusting the laser energy to the keyhole regime to remelt the former layer, which is vulnerable to keyhole pores when the local spatial energy density is too high. Excess high energy results in intensive evaporation accompanied by plasma and recoil pressure, leaving a cavity in the melt pool [2]. A keyhole pore is formed when the cavity traps gas. In LPBF, when the melt pool transforms from conduction mode to keyhole mode, which is beneficial for materials with low laser absorptivity, it is likely to generate a keyhole pore. Therefore, in-depth research on the formation mechanism of keyhole pores is required.

The development of *in situ* X-ray imaging has provided new insights into keyhole pore formation, which can be classified into three cases [2, 4, 13-17] : (1) pores were revealed during the rapid change in velocity at the turning point [2]; (2) laser shutting-off at the end of the track results in a decrease in the recoil pressure and pore production [4]; (3) unstable keyhole forms a pore when the laser is running [14]. Because the first and second cases are relatively unavoidable and fixed, this study only focuses on the third case. Huang et al. [18] performed *in situ* synchrotron X-ray imaging during LPBF and found that keyhole pores occur under high laser power-velocity conditions at the rear keyhole wall owing to the radial keyhole fluctuation (abbreviated as R-pore). Under the combination of high power and low velocity, pores are pinched off the keyhole tip and captured by the solidification front (RF-pore). However, X-ray imaging technology is limited to further analyzing the keyhole pore formation in terms of the physical information inside the melt pool, such as fluid flow and forces, owing to the high cost, massive data processing, and limited information obtained from the side of the melt pool. Alternatively, the well-validated numerical model is a cheap and reliable choice to analyze most of the involved physics information inside the melt pool, providing a better understanding of the physical mechanisms of various phenomena during the laser-matter interaction [19-24]. For example, Tang et al. [20] investigated surface defects using computational fluid dynamics and revealed the humping mechanism where capillary instability divided the swelling into separated regions under a high scanning speed. Wu et al. [21] attributed the spatter formation mechanism to two factors using a three-dimensional (3D) numerical model: the low surface tension and the upward moving melt around the keyhole accelerated by the recoil pressure and shear stress. Li [24] quantitatively investigated the gas flow, powder-gas interaction, and powder behavior under different ambient pressure levels using a 3D multi-physics model. The keyhole dynamics and melt flow behavior under sub-atmospheric pressure were explored by Li [22] with a 3D numerical model. These results indicated that a larger keyhole opening size, thinner keyhole, large melt flow velocity, and weakened vortices are responsible for the lower porosity under laser welding. The dross phenomenon during the LPBF process was studied by Charles et al. [25] *via* a multiphysics model. Its formation was attributed to the change in the melt pool regime when entering the powder with less heat transfer efficiency, leading to the drilling effect.

There are also various works on keyhole characteristics and fluid flow to correlate with keyhole pore formation. Using a physics-based model, Panwisawas [26] indicated that the periodic collapse of the keyhole and unstable fluid flow was responsible for the porosity during laser fusion welding. Khairallah et al. [27] discovered period oscillations in the melt pool depression existed before the transition to chaotic and pore-generating turbulence. The authors revealed that the physical mechanism behind this oscillation was driven by a tug-of-war between surface tension and recoil pressure *via* a high-fidelity model. Bayat et al. [28] investigated the formation of keyhole and keyhole pores using a multiphysics numerical model. The results suggested that pores were formed owing to the local cold region with insignificant recoil pressure and higher surface tension. Furthermore, these pores might float up to escape the free surface and coalesce with other pores to enlarge or even merge with the keyhole to disappear. In addition, the authors also demonstrated that the lack-of-fusion voids were formed owing to the improper fusion of the particles between the tracks [29]. Wang et al. [30] summarized the keyhole RF-pore formation mechanism into two steps using a finite volume model: (1) instant bubble formation, which can be attributed to the rear and front keyhole wall fluctuation and formation of a bridge; (2) bubble capture by solidification. A similar mechanism has been revealed by Wu [31] in the laser welding. These authors also demonstrated the R-pore formation mechanism and attributed it to the instability of the rear keyhole walls.

The above-mentioned two pore-formation mechanisms (RF-pore and R-pore) occur during the liquid–solid interaction (the keyhole is entirely surrounded by the melt). A keyhole pore can also be formed when the keyhole penetrates the melt pool (abbreviated as KP-pore) [18] [32]. However, the formation mechanism of these pores is unclear. Aluminum possesses high conductivity and low laser absorptivity [33], implying that a high laser energy density is necessary to obtain better quality. Keyholes can theoretically be treated as optical black bodies, which can significantly improve the laser absorption rate by as much as 100% [34]. The study by Ye et al. [35] revealed that the absorption rate in the deep keyhole state can be ≥ 70%, therefore, it is necessary to study the keyhole processing regime for aluminum.

Herein, a 3D thermal-mechanical-fluid coupled model was established *via* the finite volume method (FVM), considering the heat transfer, fluid flow, recoil pressure, and solidification drag model. The proposed model is validated by *in situ* X-ray imaging results, revealing the fluid flow, keyhole fluctuation, and three types of pore formation processes and mechanisms (KP-pore, RF-pore, and R-pore) under a range of high-speed welding and powder bed fusion conditions. The goal of this research is to provide a comprehensive understanding of keyhole-induced porosities in laser powder bed fusion of aluminum and suggests a strategy for pore-free laser fusion.

2. Mathematical model and numerical simulation

The interaction between laser and materials involves many physical phenomena, such as evaporation, heat transfer and mass transfer. To simplify the model, the following assumptions are necessary. (1) The shielding gas is ignored, and the area other than the fluid is treated as void with uniform temperature and pressure. (2) Phase change is taken into consideration, but the resulting compositional change is omitted. (3) The fluid is incompressible Newtonian fluid; (4) The vapor is not modeled but the effect is considered.

2.1 Governing equations

The mass transfer and heat transfer in the molten pool were calculated by solving the following three conservation equations [36]. The mass conservation equation is given as follows:

$$\nabla \cdot (\vec{v}) = 0 \tag{1}$$

where $\vec{v}$ (m· s^{-1}) is the velocity vector.

The Navier–Stokes equation is given as follows:

$$\frac{\partial \vec{v}}{\partial t} + \vec{v} \cdot \nabla \vec{v} = -\frac{1}{\rho} \nabla p + \mu \nabla^2 \vec{v} - F_d \vec{v} + \vec{G} \tag{2}$$

where ρ (kg· m^{-3}) is the density, p (Pa) is the pressure, μ (Pa· s) is the dynamic viscosity. F_d (kg $\cdot m^{-3} \cdot s^{-1}$) is the drag force coefficient and a detailed description on this will be given in section 2.2. $\vec{G}$ (m· s^{-2}) is the body acceleration due to body force.

The energy conservation equation is given as follows:

$$\frac{\partial h}{\partial t} + \vec{v} \cdot \nabla h = \frac{1}{\rho} \nabla \cdot (k \nabla T) \tag{3}$$

Where h ($J \cdot kg^{-1}$) is the enthalpy, k ($W \cdot m^{-1} \cdot K^{-1}$) is the thermal conductivity and T (K) is the temperature. The enthalpy-based continuum model is used to take the solid–liquid phase change into consideration:

$$h = \begin{cases} \rho_s C_s T, & (T \le T_s) \\ h(T_s) + h_{sl} \dfrac{T - T_s}{T_l - T_s} & (T_s < T \le T_l) \\ h(T_s) + \rho_l C_l (T - T_l) & (T_l < T) \end{cases} \tag{4}$$

where ρ_s and ρ_l (kg· m^{-3}) are the solid density and liquid density, respectively. C_s

and C_l (J$\cdot kg^{-1}\cdot K^{-1}$) are the specific heat of the solid state and liquid state at a constant volume, respectively. T_s and T_l (K) are the solidus and liquidus temperature. h_{sl} ($J\cdot kg^{-1}$) is the fusion enthalpy.

The evolution of gas-liquid free surface is tracked by the volume of fluid (VOF) method:

$$\frac{\partial F}{\partial t}+\nabla\cdot(\vec{v}F)=0 \tag{5}$$

where F is the volume of the fluid.

2.2 LPBF models

Gaussian heat source [36] is used in this simulation and given as follows:

$$q=\frac{3PA}{\pi r^2}e^{\left(\frac{-3(x^2+y^2)}{r^2}\right)} \tag{6}$$

where q ($J\cdot m^{-2}\cdot s^{-1}$) is the laser heat flux absorbed by the free surface at the point (x,y). P (W) is the power of the laser source, A is the absorption rate of the material and r (m) is radius of the laser beam spot. The algorithm for laser heating powder is to find the cell at the free surface within the laser irradiation range at every timestep and heat it. The combined effects of surface heat source, recoil pressure and VOF method can well realize the keyhole phenomenon.

The constant pressure and vaporization model is adopted to simulate the phase change and bubble formation. Vaporization will happen when the temperature of the fluid at free surface exceeds the saturation temperature at a rate given by:

$$\delta=\alpha A_{sur}\frac{k(T-T_b)}{l_hL_v} \tag{7}$$

where α is evaporation coefficient, A_{sur} (m^2) is the effective surface area for phase change, T_b (K) is the boiling point, l_h (m) is a characteristic length for heat conduction in the liquid at the surface in terms of a Prandtl number, and L_v ($J\cdot kg^{-1}$) is the latent heat of vaporization.

When a high energy laser beam irradiates on the material, it is accompanied by violent evaporation and a large amount of vapor. The metal vapor isn't modeled, but its effect, recoil pressure is included in the model. The widely accepted recoil pressure model is Clausius–Clapeyron equation [37], which can be written as:

$$P_r \cong \frac{1+\beta_R}{2} P_{atm} exp\left[\frac{L_v(T-T_b)}{TRT_b}\right] \tag{8}$$

where P_r (Pa) is recoil pressure. β_R denotes the ratio of recondensation particles to the evaporation ones, P_{atm} (Pa) represents ambient pressure and R $(J \cdot kg^{-1} \cdot K^{-1})$ is gas constant. However, this equation suits the situations that ambient pressure has no influence on the evaporation process or vapor pressure is far larger than the ambient pressure. Nevertheless, there is report demonstrating that ambient pressure confines the evaporation process and increase β_R [38]. Pang et al. [39] proposed a modified recoil pressure model that uses surface pressure to cover the effect of ambient pressure. For a given ambient temperature, when the temperature is lower than the boiling point, the surface pressure equals to the ambient pressure. For a higher temperature, Clausius–Clapeyron equation is used to calculate the surface pressure. Taking the ambient pressure as the zero level of pressure, the recoil pressure can be expressed as: $P_r = P_s - P_{atm}$. The surface pressure model used in this study can be expressed as:

$$P_s = \begin{cases} P_{atm} & 0 \le T < T_b \\ \frac{1+\beta_R}{2} P_{atm} exp\left[\frac{L_v(T-T_b)}{TRT_b}\right] & T_b \le T < \infty \end{cases} \tag{9}$$

Mush zone is a region that solid and liquid coexist as a mixture. Solidification implies a rigidity and resistance to the fluid flow, resulting in the fluid velocity sharply changed. The *in-situ* experiment conducted by Zhao et al. [15] demonstrated that solidification drag force has an effect on the formation of keyhole pore. Thus, the Darcy drag force model is implemented in current study to characterize the effect of drag force in the molten pool [30]. The solidification process is approximated by a drag force coefficient F_d, which is a function of the local solid fraction. It can be written as:

$$F_d = TSDRG \frac{F_s^2}{B+(1-F_s)^3} \tag{10}$$

$$TSDRG = \frac{180\mu}{\lambda_1^2 \rho} \tag{11}$$

where $TSDRG$ represents a coefficient related with the mush zone microstructure, F_s is the local solid fraction, B is the positive zero used to avoid the division by zero. λ_1 (m) is the characteristic length of mush zone.

2.3 Computational domain and boundary conditions

The developed model is shown in **Fig. 1**. The powder bed is modeled *via* Particle

Flow Code (PFC) commercial software and its built process is shown in **Fig. 2**. The diameter of the particle is in the range of 22-50 μm and the layer thickness is 30 μm. Uniform hexahedral grid geometry with a size of 6 μm is used in the simulation, which can provide sufficient high-precision fluid after the mesh-sensitivity analysis. A time-step controlled by stability and convergence is adopted, which is around 0.068 μs after the time-step dependence analysis. The parameters for sensitivity analysis are given in **table s2** in supplementary information. The full data for heat and mass transfer is recorded every 1 μs. The simulation is carried out *via* the commercial software Flow 3d v11.2.

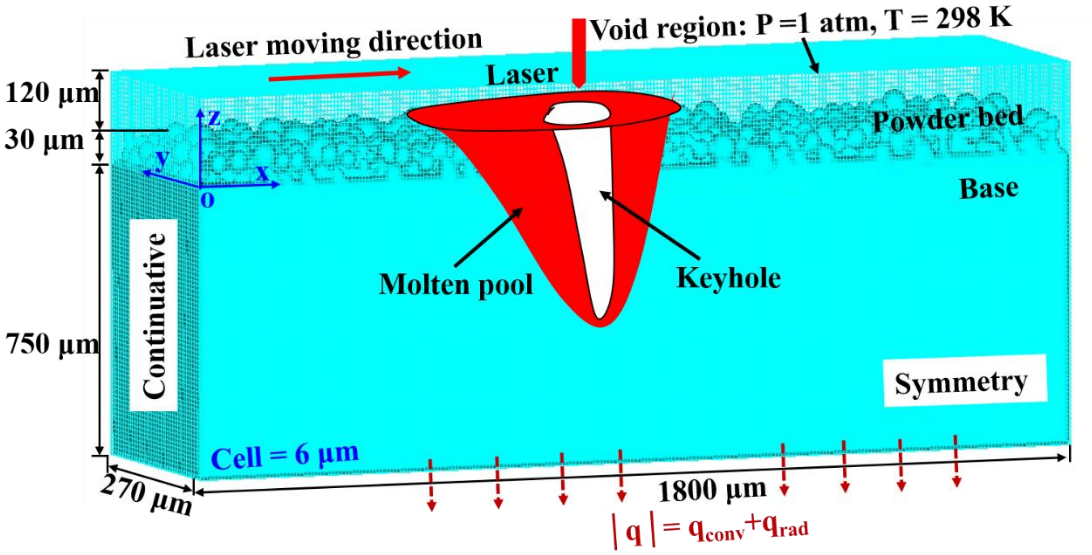

Fig. 1 Computational domain and boundary condition

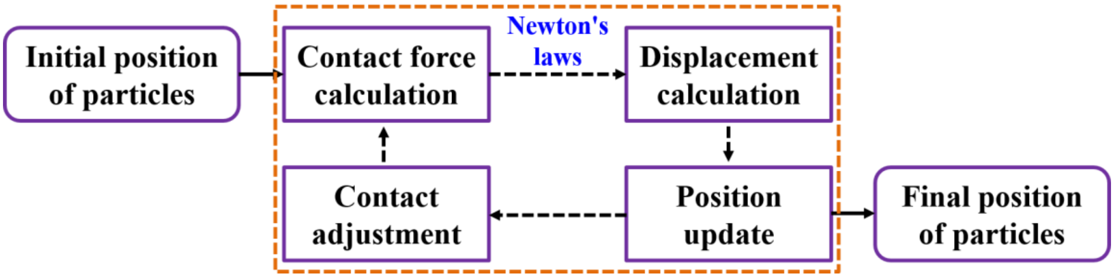

Fig. 2 Powder bed generation process

The heat source is regarded as part of the surface heat flux boundary condition, and the main energy transfer modes in the upper free surface include convection, radiation and evaporation, which can be expressed as:

$$k\frac{\partial T}{\partial \vec{n}} = q - q_{conv} - q_{rad} - q_{evap} \tag{12}$$

$$q_{conv} = h_c(T - T_a) \tag{13}$$

$$q_{rad} = \sigma\varepsilon(T^4 - T_a^4) \tag{14}$$

$$q_{evap} = \varphi L_v P_{atm}\sqrt{\frac{1}{2\pi RT}}exp\left[\frac{L_v(T - T_b)}{TRT_b}\right] \tag{15}$$

Where $\vec{n}$ is the surface normal vector and h_c ($\mathrm{W} \cdot m^{-2} \cdot K^{-1}$) is the heat transfer coefficient. T_a (K) is the reference temperature. σ ($\mathrm{W} \cdot m^{-2} \cdot K^{-4}$) is the Stefan-Boltzmann constant and ε is the radiation emissivity. For other surfaces, only convection and radiation are considered.

$$k\frac{\partial T}{\partial \vec{n}} = -q_{conv} - q_{rad} \tag{16}$$

The pressure boundary condition on the upper surface can be written as:

$$-p + 2\mu\frac{\partial \vec{v}_n}{\partial \vec{n}} = -P_r + \frac{\gamma}{R_k} \tag{17}$$

where $\vec{v}_n$ ($\mathrm{m} \cdot s^{-1}$) denotes the normal velocity vector. γ ($\mathrm{N} \cdot m^{-1}$) and R_k (m) are the surface tension and the radius of curvature, respectively. The thermophysical properties for pure aluminum used in this study were calculated by JmatPro software [36, 40], displayed in **Fig. 3**. The thermal and mechanical parameters for LPBF simulation of aluminum are shown in **Table 1**. The laser parameters can be found in **Table s2** in supplementary document.

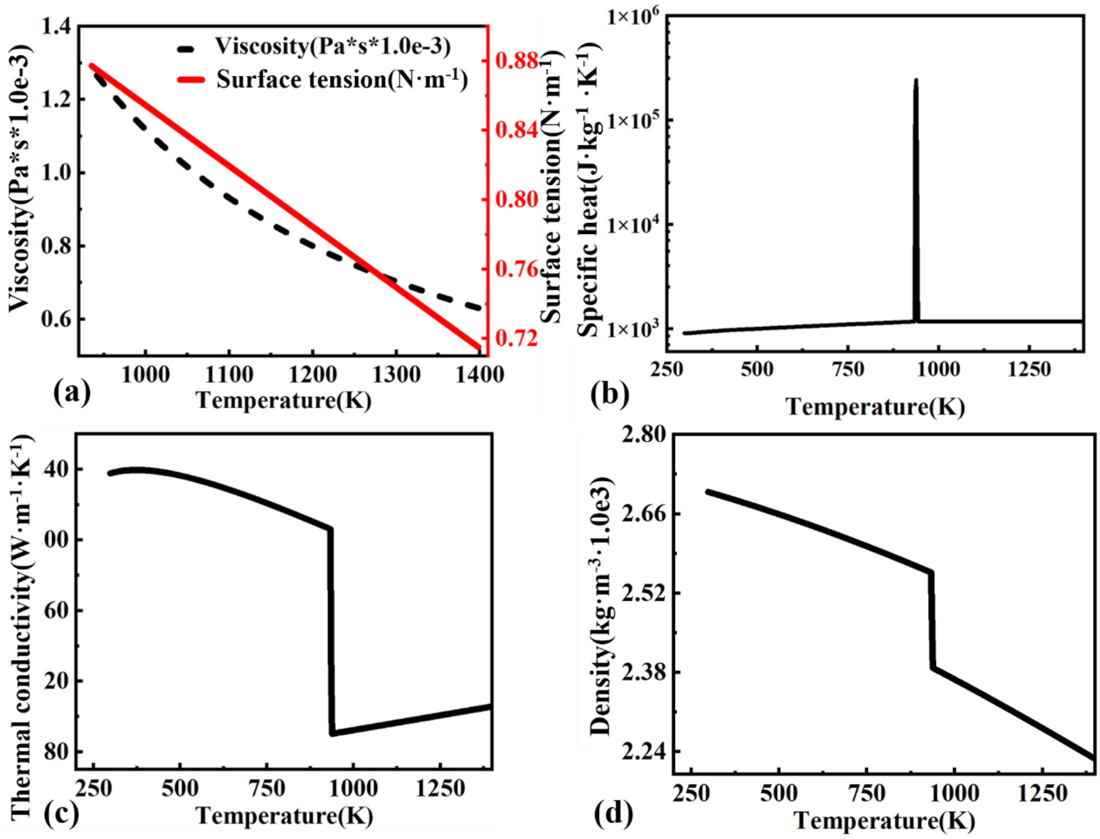

Fig. 3 Thermophysical properties of pure aluminum used in the simulation calculated by JmatPro software: (a) viscosity and surface tension, (b) specific heat, (c) thermal conductivity, (d) density.

Table 1 Thermal and mechanical parameters for LPBF simulation of aluminum

Properties	Value
Coefficient of evaporation α	0.01
Latent heat of vaporization L_v (J· kg^{-1})	1.077·E+07
Gas constant R (J· kg^{-1}· K^{-1})	308
Ambient pressure P_{atm} (Pa)	101300
Convective heat transfer h_c (W· m^{-2}· K^{-1})	80
Reference temperature T_a (K)	298
Stefan-Boltzman constant σ (W· m^{-2}· K^{-4})	5.67E-08
Radiation emissivity ε	0.36
Boiling temperature T_b(K)	2750

Melting temperature (K)	933
Laser absorption	0.7
Recondensation coefficient β_R	0.5795 [41]
Characteristic length of mush zone λ_l (μm)	5 [42]

3. Results and discussion

To ensure the validity of the simulation results, the parameters used in this model for the pure aluminum substrate were the same as those adopted in the *in situ* LPBF experiment reported by Huang et al. [18]. **Fig. 4** shows a comparison of the keyhole morphology obtained by high-speed X-ray imaging [18] and the numerical simulation in this study. The depth and morphology of the keyhole were consistent, indicating the model validation data.

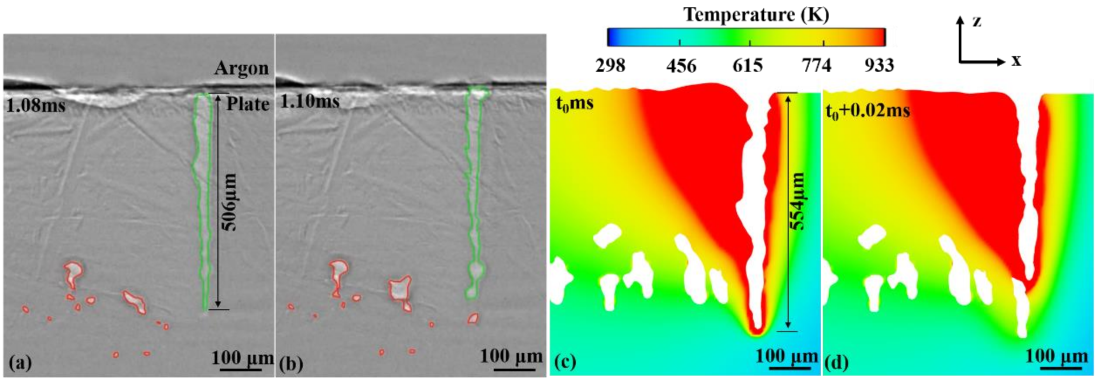

Fig. 4 Comparison of the keyhole morphology obtained by (a, b) X-ray imaging (adapted with permission from ref. [18]) and (c, d) simulation. The laser power is 500 W, scanning speed is 600 mm·s^{-1} and the spot diameter is 50 μm. Laser moves from left to right.

Three types of keyhole pores (KP-pore, RF-pore, and R-pores) were reproduced in this simulation. As the KP-pore was realized by simulation for the first time, a detailed description of its formation process and mechanism will be provided.

3.1 KP-pore formation process

KP-pore results from keyhole penetrating molten pool. A bubble could be formed during gas–solid interaction. **Fig. 5** shows the entire KP-pore formation process. In the first (i) stage, the main fluid flow in the molten pool behind the keyhole includes upward flow along the edge of the molten pool (1), clockwise flow (2), and backward flow in the upper part of the melt pool (3). The collision of flows 1 and 3 generates a hump on the upper surface of the rear part of the molten pool. Fluid 2 has a horizontal velocity, leaving a bulge at the rear keyhole wall. Similarly, a bulge appears at the front keyhole wall when the upward flow (4) and downward flow (5) collides in the former part of the melt pool. Because the bulges are closer to the laser beam center, which possesses the highest energy density, they are strongly irradiated, leading to local heat accumulation at temperatures much higher than the boiling point. The surface tension decreases sharply as the temperature increases, whereas the recoil pressure increases exponentially [2, 27], which dominates the fluid flow and pushes the bulges downward. As the bulges block part of the laser radiation, only the laser beam passing through the middle of the bulges can reach the keyhole bottom, causing local evaporation and increasing the keyhole depth. Meanwhile, the area of the keyhole sidewall solidifies gradually.

In the second (ii) stage, the middle part of the keyhole is gradually captured by the solidification interface, whereas the bottom part is still subjected to laser irradiation and thus increases the keyhole depth. The hydrostatic pressure in the upper rear of the molten pool becomes larger than the Marangoni effect owing to the accumulation of fluid, and flow 3 gradually flows forward (3′). The downward and upward flows at the front keyhole wall continue to form a bulge.

In the third (iii) stage, as the frozen part is outside of the laser irradiation, the upward flows at the rear and front keyhole wall have horizontal velocities towards the keyhole as they reach the frozen region and then a liquid bridge forms, resulting in the keyhole bottom quickly being captured by the solidification interface. The bridge is subjected to strong laser radiation, and the dominant recoil pressure forces it to break (stage iv at 0.346 ms). Subsequently, the bubble is captured by the keyhole. A valley gradually appears in front of the hump owing to the forward flow 3′.

In the stage v, the main flow direction includes upward flow along the fusion line of the molten pool (1), clockwise flow (2), forward flow (3′) and downward flow (5). As flow 2 and flow 3′ are two fluids with different strengths, the collision on the rear keyhole wall induces a bulge. The bulge around the keyhole reduces the keyhole diameter and results in a phenomenon similar to necking, blocking the part of the downward laser irradiation. The sidewall of the lower part of the keyhole is gradually captured by the liquid–solid (L/S) interface. Influenced by the solidified region, the downward flows generate horizontal velocities towards the keyhole, forming two liquid bridges, then a pore and a bubble, which can be seen at 0.358 ms. The high recoil pressure acting on the upper bridge forces it to break and the bubble is captured by the keyhole. The lower pore is completely retained in the material.

Our simulation results indicate that the pore formation process takes approxomately 40 μs and matches the X-ray imaging results [18]. The formation of the KP-pore is due to the continuous bulges at the keyhole wall, leading to the fluctuation and rapid solidification of the keyhole bottom. Finally, a pore is completely left in the material under the condition that the keyhole penetrating the molten pool. We also noticed the similar pore formation process in the video of *in-situ* X-ray imaging by Huang et al. [18], as shown in **Fig. 5** (d). At 0.72 ms, the keyhole penetrated the melt pool, and the fluid could not effectively fill the void region at the tip. Therefore, pores were more likely to be generated during subsequent keyhole fluctuations. It was also observed that the position and shape of this type of pore were unchanged before and after its formation. This is because such pores are generated by the keyhole penetrating the melt pool; thus, they are captured by the L/S interface before its formation.

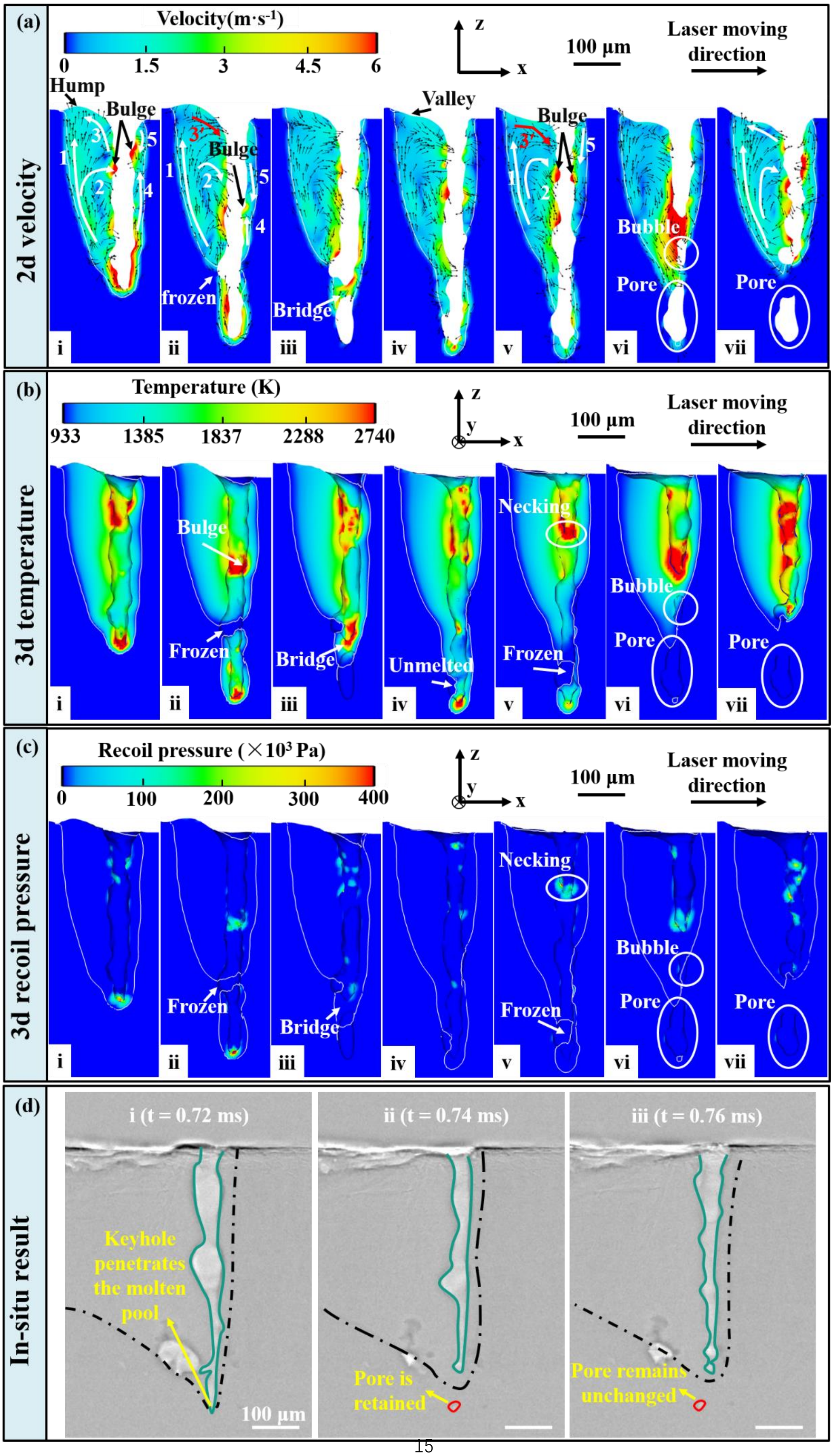

(a)
2d velocity
Velocity(m·s-1)
0
1.5
3
4.5
6
z
x
100 μm
Laser moving direction
Hump
Bulge
Valley
Bulge
frozen
Bridge
Bubble
Pore
Pore
i
ii
iii
iv
v
vi
vii
(b)
3d temperature
Temperature (K)
933
1385
1837
2288
2740
z
y
x
100 μm
Laser moving direction
Bulge
Frozen
Bridge
Unmelted
Necking
Frozen
Bubble
Pore
Pore
i
ii
iii
iv
v
vi
vii
(c)
3d recoil pressure
Recoil pressure (×10³ Pa)
0
100
200
300
400
z
y
x
100 μm
Laser moving direction
Frozen
Bridge
Necking
Frozen
Bubble
Pore
Pore
i
ii
iii
iv
v
vi
vii
(d)
In-situ result
i (t = 0.72 ms)
ii (t = 0.74 ms)
iii (t = 0.76 ms)
Keyhole penetrates the molten pool
Pore is retained
Pore remains unchanged
100 μm

Fig. 5 Fluid flow and formation of KP-pore in the longitudinal plane. (a) 2D clips of velocity, 3D clips of (b) temperature and (c) recoil pressure, (d) X-ray imaging of KP-pore formation (adapted with permission from ref. [18]). Note, the temporal resolution of X-ray imaging (20 μs) might be insufficient to capture the whole penetration dynamics, therefore, we are unable to fully verify the model. The labels i−vii indicate the moments of 0.317, 0.330, 0.336, 0.346, 0.350, 0.358, and 0.364 ms, respectively. The arrows 1−5 in (a) represents the fluid flow direction. The red circles in (d) denote the pores. The white lines in (a)–(c) and the black dotted line in (e) show the L/S interface. The laser power is 500 W, the scanning speed is 600 mm/s, and the spot diameter is 50 μm.

As the KP-pore occurs when the keyhole penetrates the melt pool, its depth was extracted and analyzed, as shown in **Fig. 6**. The L/S interface velocity of the molten pool tip was calculated based on equation (c). A positive L/S velocity indicates the melting process, whereas a negative value indicates the solidification process. The keyhole tip was captured by the L/S interface when the keyhole had a greater depth than the molten pool. Under such conditions, if bulges appear on the keyhole wall and the laser energy entering the keyhole is reduced, the bottom will solidify quickly and form a pore. If more laser beam is in, the tip of the keyhole may be remelted and thus capture the existing pores. The effects of the depth difference and L/S interface velocity on the KP-pore formation are shown in **Fig. 6** (d). A higher velocity indicates faster-molten pool expansion and more molten metal, indicating a lower chance of leaving a pore. In contrast, pores are more likely to occur at a greater penetration depth (lower left corner). It is apparent that when the keyhole penetrates the molten pool, pores are easily generated, except for the region in the upper-right corner, which may be desired in the printing process. The corresponding pores are shown in **Fig. 10** (g).

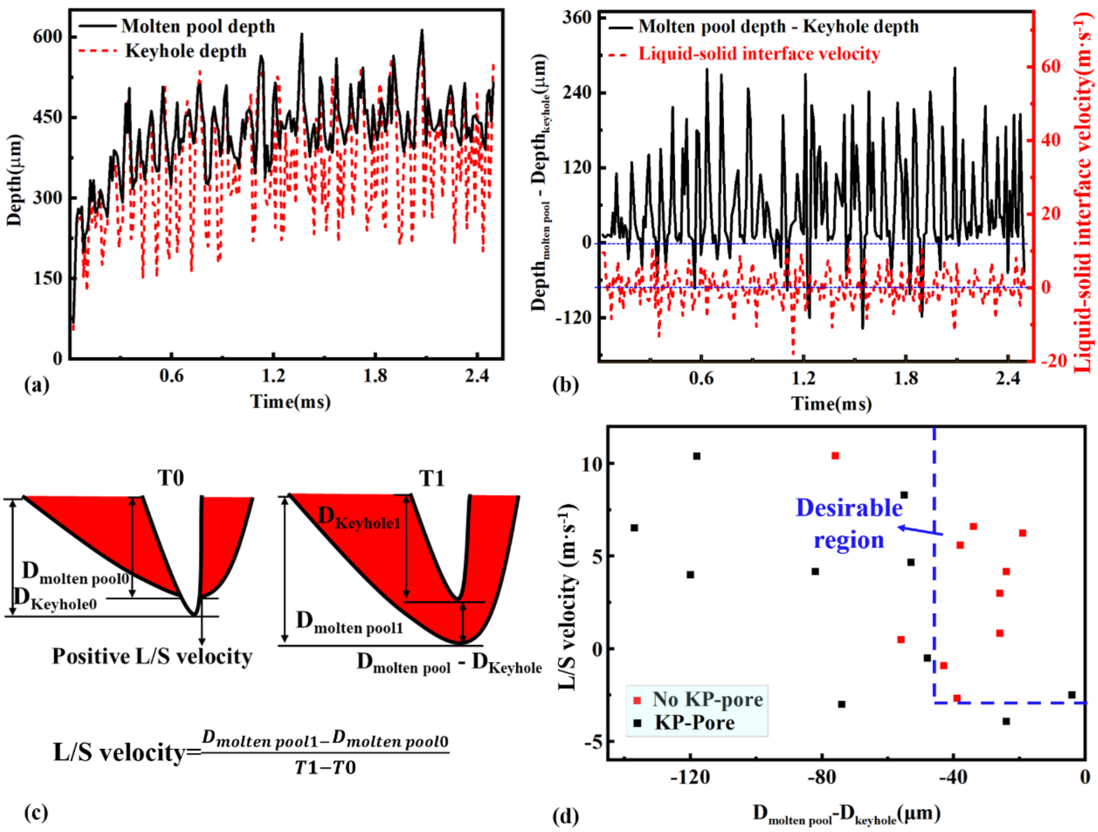

Fig. 6 (a) Depth of the molten pool and keyhole. (b) Depth difference and the L/S interface velocity in vertical. The data is extracted every 12 μs. (c) Schematic of the extracted feature parameters. (d) Effects of depth difference and L/S interface velocity on KP-pore formation.

3.2 Formation mechanism of KP-pore

To show the influence of fluid flow on keyhole fluctuation, a 3D streamline was extracted, as shown in **Fig. 7** (a). Bulges are formed owing to the clockwise flow 2 hitting the rear keyhole wall and the collision of upward flow 4 and downward flow 5, resulting in necking and damping of the laser irradiation. The bottom of the molten pool rapidly solidifies, and the temperature of the sidewall at the lower part of the keyhole decreases below the boiling point. However, the keyhole depth increases as the laser passing through the necking can reach the tip. At 0.336 ms, the downward flows in the molten pool generate horizontal velocity as they reach the frozen zone, forming a liquid bridge between the rear and front keyhole walls and leaving a pore. Nevertheless, the bulges gradually disappear under intense evaporation, and the pores are captured by the keyhole. As the flow is unstable, it continuously hits the keyhole wall and forms bulges, causing keyhole fluctuations. Eventually, a pore is generated at the keyhole tip when it penetrates the melt pool.

Fig. 7 (b) displays a schematic of the KP-pore formation mechanism, which can be divided into four steps. (I) For the molten pool behind the keyhole, upward flow 1 along the fusion line and backward flow 3 leave a hump at the upper surface of the rear of the melt pool, whereas clockwise flow 2 hits the rear keyhole wall and generates a bulge. For the molten pool in front of the keyhole, the collision of upward and downward flows also forms a bulge. The bulges around the keyhole reduce the keyhole diameter and result in necking, hindering the downward irradiation of the laser. (II) As the energy entering the keyhole significantly decreases, the bottom of the molten pool quickly solidifies, and a part of the keyhole is captured by the L/S interface. The keyhole depth further increases owing to the laser beam passing through the necking. At this moment, backward flow 3 gradually changes its direction to forward flow 3′ as the hydrostatic pressure is greater than the Marangoni effect owing to the formation of the hump. (III) Owing to the unstable fluid flow, bulges continuously form and disappear, resulting in the keyhole bottom being gradually captured by the solidification interface; that is, the keyhole penetrates the melt pool. It is a gas -solid interaction, instead of the previously reported liquid–solid interaction that keyhole is surrounded by the liquid and then pinning off a bubble [15, 30] . Because of the forward flow 3′, a valley appears ahead of the hump. (IV) When the keyhole depth exceeds the molten pool depth, a pore will likely form when the keyhole fluctuates. The morphology of this type of pore is consistent with the shape of the keyhole tip because it is prematurely captured by the solidification interface.

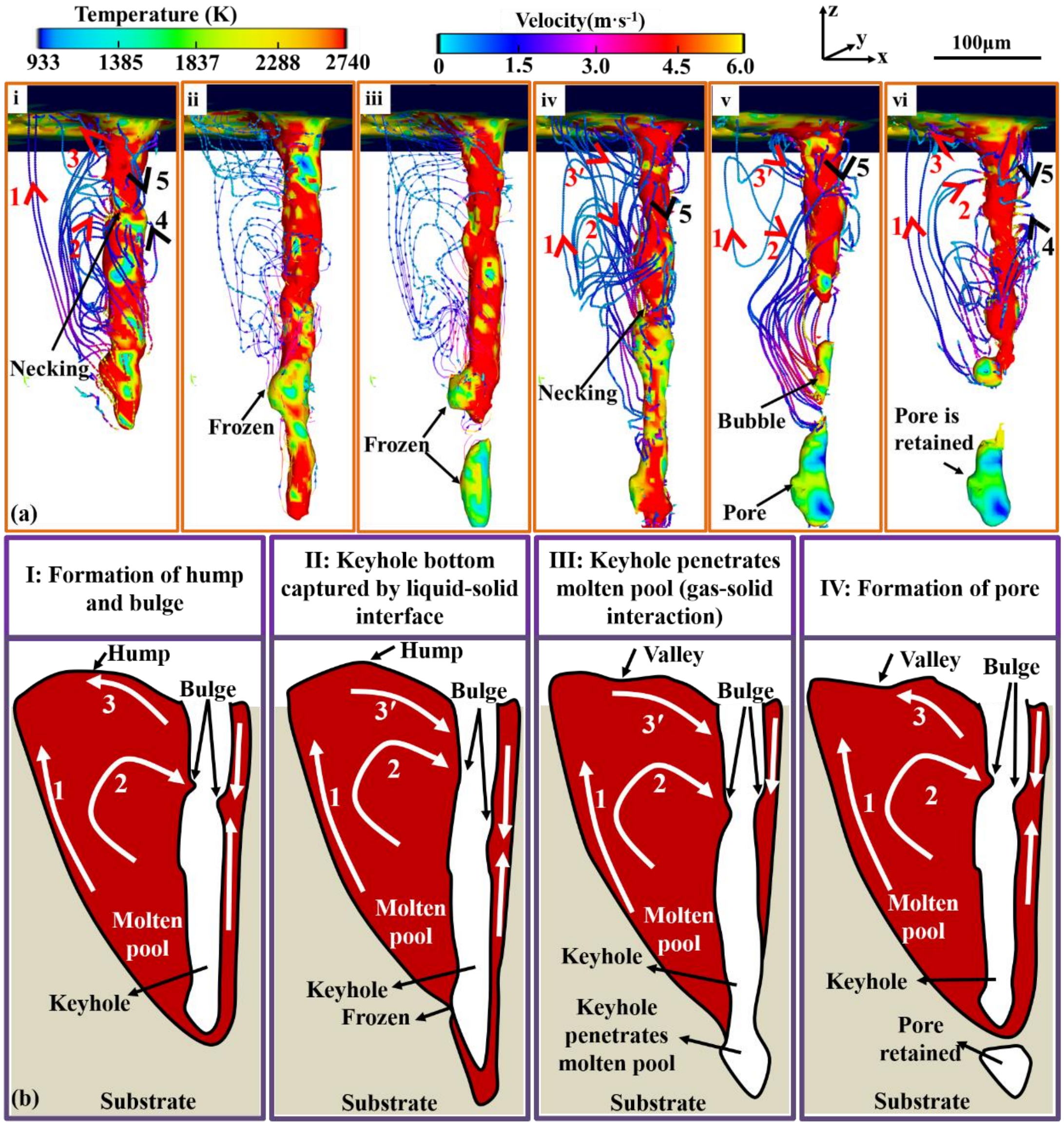

Fig. 7 (a) 3D streamlines showing the keyhole and pore evolution. (b) Schematic showing the KP-pore formation mechanism in which the KP-pore is formed during the gas-solid interaction. The laser moves along the positive direction of the X-axis. The labels i–vi in (a) denote the moments at 0.317, 0.330, 0.336, 0.350, 0.358, and 0.364 ms, respectively. The V-shaped red and black arrows in (a) represent the fluid flow directions in the melt pool behind and in front of the keyhole, respectively.

As R-pore and RF-pore have been extensively investigated very well [18, 30, 31], only a brief discussion is provided in this study.

3.3 Formation of RF-pore

Fig. 8 displays snapshots of the fluid flow and the formation dynamics of RF-pore in the longitudinal plane. The fluid in the molten pool behind the keyhole flows forward owing to the effects of hydrodynamic and hydrostatic pressure and surface tension, acting as a force to close the keyhole (**Fig. 8** (i)). Similarly, the fluid on the front wall of the keyhole also flows backward. Nevertheless, the recoil pressure resulting from evaporation prevents this process. Under the combined action of these forces, the fluid at the rear and front keyhole wall repeats this process: bulge formation→ liquid bridge formation→ liquid bridge broken. At 1.402 ms, the fluid between the front and rear keyhole wall forms a bridge again. The keyhole then pinches off a cavity to form a gas bubble (**Fig. 5** (iii)). It moves with the clockwise flow in the molten pool behind the keyhole and finally gets captured by the L/S interface (**Fig. 5** (vi)). The mechanism of this type of bubble has been described as the formation of an instant bubble and pinning on the solidification interface [30]. It is apparent that such a pore is formed during the liquid-solid interaction and its dynamics are primarily affected by surface tension. This is because most of the bubble's lifetime is surrounded by fluid; thus, it will gradually adjust its shape to achieve the lowest surface energy, which is spherical or nearly spherical. For this pore, there is generally a rough time period of 200 μs for the bubble to fully adjust the shape before being fully captured by the S/L boundary.

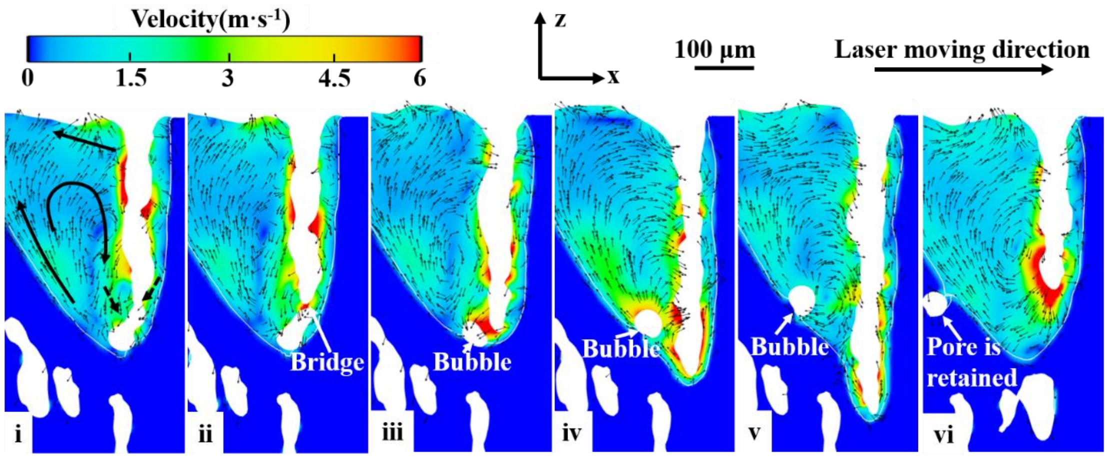

Fig. 8 Fluid flow and formation of RF-pore in the longitudinal plane. The labels i–vi indicate the moments of 1.401, 1.402, 1.417, 1.431, 1.472, and 1.608 ms, respectively. The black solid line in the first picture on the left represents the direction of fluid flow, and the black dashed line represents the flow trend of the fluid. The white line shows the L/S interface. The laser power is 500 W, the scanning speed is 600 mm/s, and the spot diameter is 50 μm.

3.4 Formation of R-pore

The second type of pore is R-pore. As described above, the recoil pressure promotes keyhole opening while the surface tension, hydrodynamic pressure, and hydrostatic pressure try to close the keyhole. At 2.234 ms (**Fig. 9** (i)), a concave shape appeared at the rear keyhole wall owing to the fluctuation. The main fluid flow direction in the rear molten pool was clockwise. Under the effect of the forces that close the keyhole, the rear keyhole wall fluctuates and then collapses and pinches off the bubble, which is relatively small and confined to the length of the rear keyhole wall. These bubbles were unstable and disappeared in most cases. The formation mechanism of the R-pore can be concluded as follows: 1) hump or budge forms at the rear keyhole wall; 2) rear keyhole wall collapses and pinch-off bubbles. Similar observations were reported in LPBF experiments [18] and welding simulation [31].

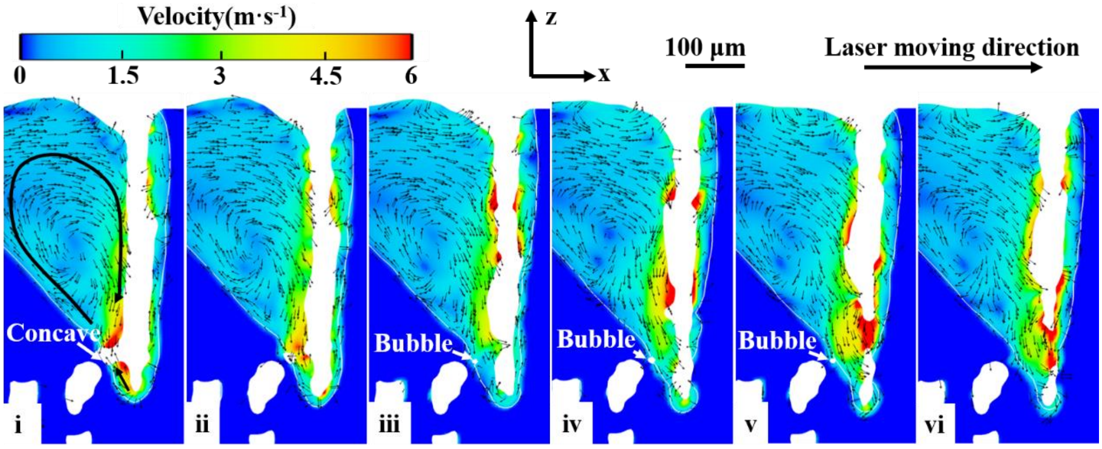

Fig. 9 Fluid flow and formation of R-pore in the longitudinal plane. The labels i–vi indicate the moments of 2.234, 2.236, 2.240, 2.242, 2.250, and 2.251 ms, respectively. The solid line in the first picture on the left represents the clockwise flow of fluid. The white line shows the L/S interface. The laser power is 500 W, the scanning speed is 600 mm/s, and the spot diameter is 50 μm.

3.5 The effect of powder on the pore

Cunningham et al. [43] and Zhao et al. [15] demonstrated that the interaction between the laser and powder promotes keyhole fluctuations. It is of great importance to explore the influence of the powder on the characteristics of the molten pool and keyhole, as well as pore formation. The thickness of the powder bed was 30 μm, and the other processing parameters were the same as those for the bare pure aluminum substrate.

Fig. 10 (a) shows that both the melt pool depth and keyhole depth with powder are lower than those of the bare aluminum substrate in **Fig. 6** (a). The powder and bulk materials are solid-state forms of the same substance and with same thermal conductivity. The main difference between them is their structures. One difference is that the powder undergoes point-to-point heat transfer, and the other is that lots of voids exist in the powder material. The combined effect of the two leads to a lower heat transfer efficiency of the powder. In practice, spattering or ablation also removes part of the laser heat, resulting in less energy being absorbed by the molten pool, and thus a smaller depth of the molten pool. This phenomenon was also reported by Zhao et al. [15] and Bobel et al. [44]. The oscillation frequency is introduced to quantitatively characterize the effect of the powder on the molten pool and keyhole characteristics. It is defined as the times the keyhole penetrated the molten pool in one second. Note that data were extracted every 12 μs. The oscillation frequency with powder (**Fig. 10** (b)) and that without powder (**Fig. 6** (b)) were counted and compared, as shown in **Fig. 10** (d). This indicates that the powder affects the laser path and increases the oscillation frequency, leading to a higher porosity. However, the pores are smaller, which may be related to the smaller keyhole depth. Actually, the results by Huang [18] and Zhao et al. [15] also indicates that powder will promote the formation of keyhole pore as well as enlarge the stable region in the process map, respectively. **Fig. 10** (e) and (f) show the three types of pore distributions. The percentages of R-bubbles, RF-bubbles, and KP-bubbles in the powder were 16.7%, 16.7%, and 66.6%, respectively. The values for the bare plate were 12.4%, 18.8%, and 68.8%, respectively. The R-bubble is small and tends to be distributed in the top region. The RF-bubble is medium-sized, nearly spherical, and primarily distributed in the middle part. The KP-bubble is large and irregular, located at the bottom, which is related to its formation mechanism.

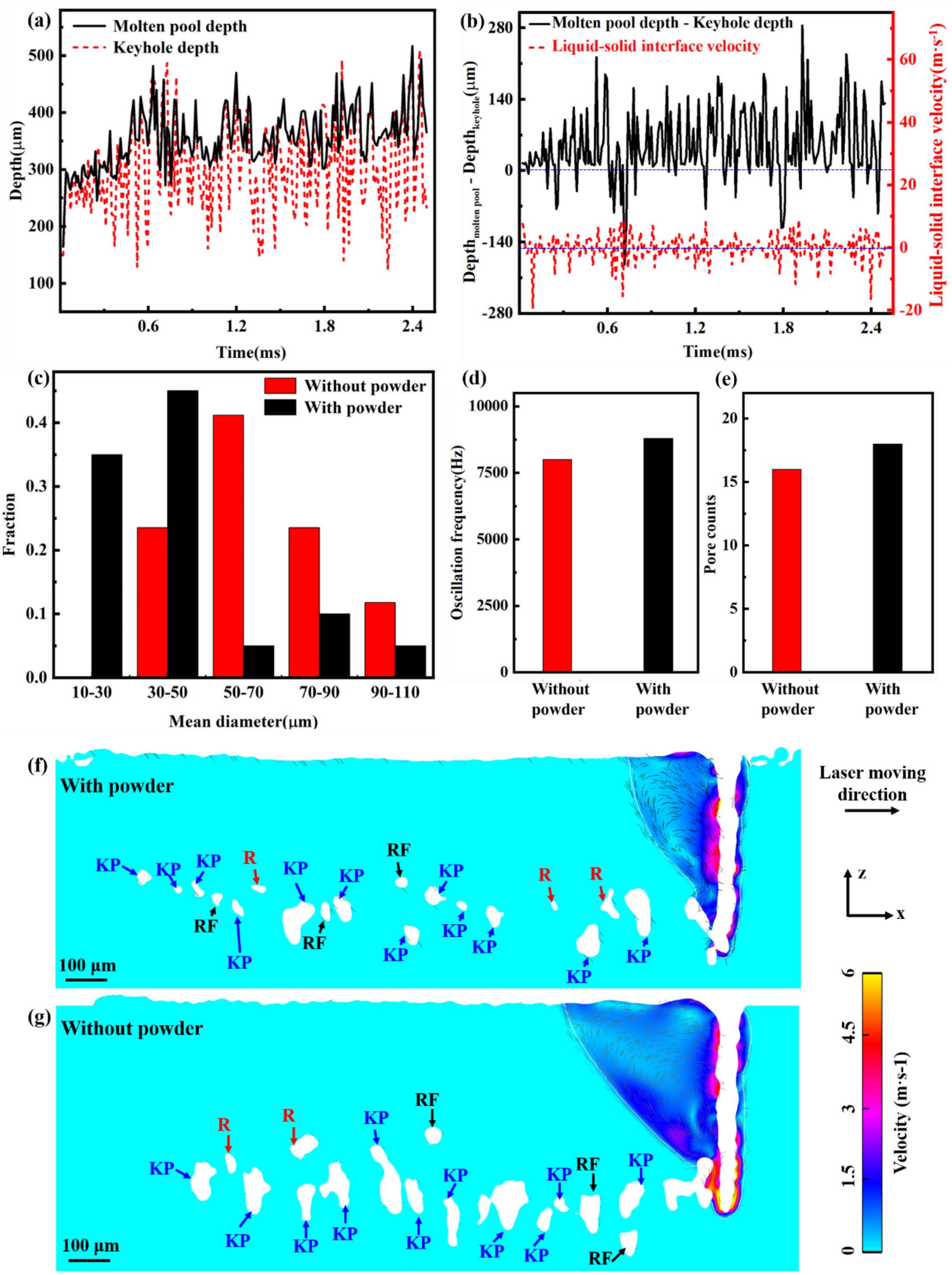

Fig. 10 Effect of powder on the (a) depth of molten pool and keyhole, (b) depth difference and L/S interface velocity, (c) pore sizes, (d) oscillation frequency and (e) KP-bubble counts. The depth data is extracted every 12 μs. (f) and (g) show the pore distribution with and without powder, respectively. The oscillation frequency represents the number of keyholes penetrating the molten pool in one second. The laser power is 500 W, the scanning speed is 600 mm/s, and the spot diameter is 50 μm.

3.6 Effect of laser energy density

As the occurrence of keyhole is closely related to the laser energy intensity ($\frac{4P}{\pi d^2}$), there is a critical threshold, beyond which keyhole forms [34]. However, most pores under a high laser energy density are owing to the instability of the keyhole. It is important to investigate the effect of laser parameters on the characteristics of the molten pool and keyhole, as well as the formation of pores. The keyhole penetrating the molten pool accounts for the KP-pore; thus, their depths are extracted, and the depth differences are obtained, as shown in **Fig. 11**. The maximum penetration depth and the times the keyhole penetrates the molten pool increases with increasing laser power. However, they decrease with increasing laser spot diameter and scanning speed. To simultaneously characterize the effects of laser energy density and scanning speed on pore formation, the linear input energy density E ($E = \frac{4P}{V\pi d^2}$) is introduced, which is confirmed to be a meaningful thermodynamic metric for LPBF to estimate the threshold of unstable keyhole by I. Bitharas et al. [45]. The effects of input energy density on the characteristics of keyhole and molten pool as well as pore formation are shown in **Fig. 12.**

Apparently, with the increase in input energy density, the oscillation frequency rapidly increases at first and then slows down (**Fig. 12** (a)). The relationship between the oscillation frequency and the input energy density can be fitted as y = $-4344564 + 4355500 \times x^{0.0007}$. R^2 equals to 0.85636, indicating a good fit. The right enlarged picture clearly demonstrates a threshold (0.026MJ·cm^{-3}) above which keyhole will penetrate the molten pool and the oscillation frequency will also rapidly increase. The input energy density is divided into two regions. Below this threshold, it is a stable energy-density combination, whereas above this threshold, it is an unstable combination. The maximum penetration depth shows similar trend to that of the oscillation frequency, and the fitted curve is y = $-251 + 461 \times x^{0.16}$, with R^2 = 0.99. The relationship between the KP-pores and the input energy density is fitted as y = $-114 + 134 \times x^{0.05}$, with R^2 = 0.99. With the increase of input energy density, the number of KP-pores rapidly increases and then slowly decreases. Similarly, there is a threshold for the KP-pore formation. Near this threshold, rapidly increases and then slowly decreases. Below this threshold, KP-pores no longer appear. The total pore count has a similar trend to the KP-pore count, which can be attributed to the fact that the KP-pore accounts for the majority of pores under high input energy density. It can also be seen from the enlarged images that the thresholds of the oscillation frequency and the maximum penetration depth are the same. The slight deviation can be attributed to the error in the curve fitting. The relationship between these four input-energy-density thresholds is in the following order: $E_{\text{Total pore counts}} < E_{\text{Oscillation frequency}} \approx E_{\text{Maximum penetration depth}} < E_{\text{KP-pore counts}}$. This is because, in the case of no penetration, RF-pore and R-pore may be generated. In contrast, KP-pore is not necessarily generated even if penetration occurs, which depends on the dynamic characteristics of the molten pool. The fitted thresholds are lower than the input energy densities used in our simulation without penetration or pore generation. Therefore, we can reasonably propose that no pores will be formed when the input energy density is below 0.02 MJ·cm^{-3}.

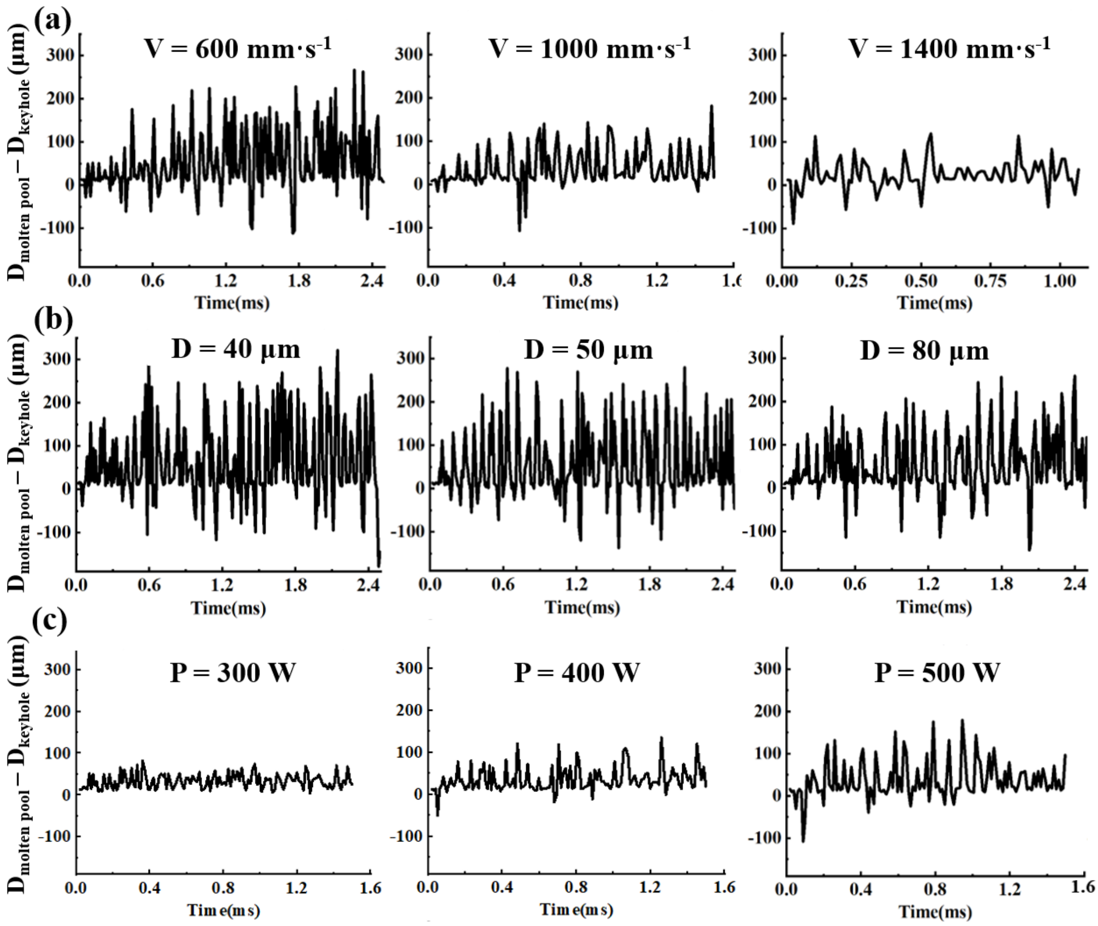

Fig. 11 Effects of (a) different scanning speeds with P = 400 W and d = 50 μm, (b) different laser spot diameters with P = 500 W and V = 600 mm·s^{-1} and (c) different laser powers with V = 1000 mm·s^{-1} and d = 80 μm on the depth differences between molten pool and keyhole.

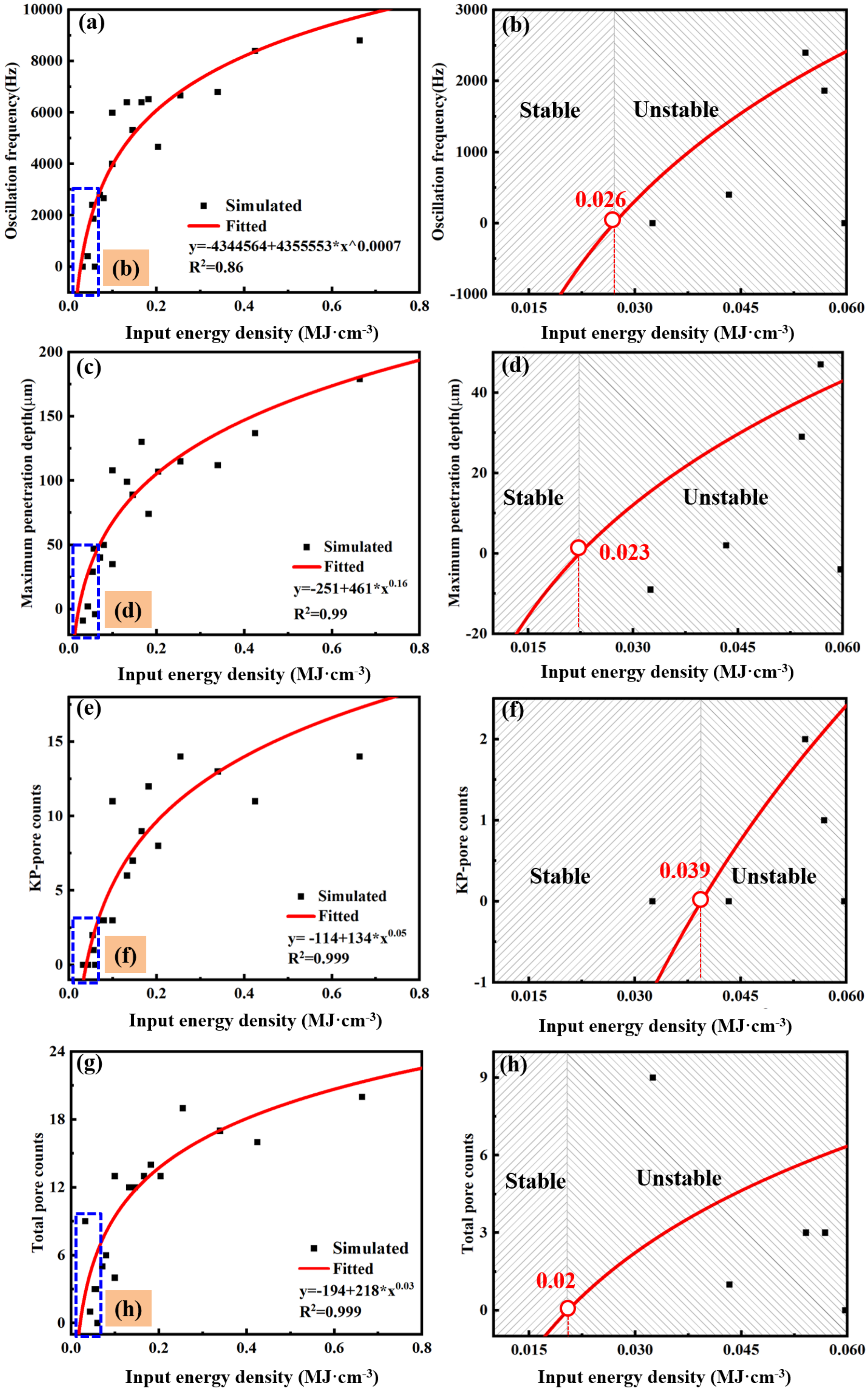

(a)
Oscillation frequency(Hz)
Simulated
Fitted
y=-4344564+4355553*x^0.0007
R^2=0.86
(b)
Input energy density (MJ·cm^{-3})
(b)
Stable
Unstable
0.026
Oscillation frequency(Hz)
Input energy density (MJ·cm^{-3})
(c)
Maximum penetration depth(μm)
Simulated
Fitted
y=-251+461*x$^{0.16}$
R^2=0.99
(d)
Input energy density (MJ·cm^{-3})
(d)
Stable
Unstable
0.023
Maximum penetration depth(μm)
Input energy density (MJ·cm^{-3})
(e)
KP-pore counts
Simulated
Fitted
y= -114+134*x$^{0.05}$
R^2=0.999
(f)
Input energy density (MJ·cm^{-3})
(f)
Stable
0.039
Unstable
KP-pore counts
Input energy density (MJ·cm^{-3})
(g)
Total pore counts
Simulated
Fitted
y=-194+218*x$^{0.03}$
R^2=0.999
(h)
Input energy density (MJ·cm^{-3})
(h)
Stable
Unstable
0.02
Total pore counts
Input energy density (MJ·cm^{-3})

Fig. 12 Effect of input energy density on the (a) (b) oscillation frequency, (c) (d) maximum penetration depth, (e) (f) KP-pore counts and (g) (h) total pore counts. The pictures on the right represent the enlarged views of the blue dashed box in the left pictures. Red open circles represent the threshold of the fitted curves without keyhole penetrating melt pool or pore formation. The input energy density E is defined as $E = \frac{4P}{V\pi d^2}$. The oscillation frequency refers to the times the keyhole penetrates the molten pool within one second. The negative maximum penetration depth means the keyhole depth is less than that of the molten pool.

Conclusion

In this study, different keyhole pore formation mechanisms were investigated using a 3D multiphysics FVM model validated by ultra-high-speed *in situ* X-ray imaging results. The main conclusions drawn are summarized as follows:

1) A new KP-pore formation mechanism is uncovered. This phenomenon occurs when the keyhole penetrates the molten pool owing to its fluctuation, resulting in keyhole pore formation during the gas–solid interaction.
2) The RF-pore and R-pore are reproduced, which has been revealed before as R-pores are generated owing to hump or budge forming at the rear keyhole wall, and the wall collapses and pinches off the bubble. The RF-pore formation results from the fluctuation and the bridge formed between the rear and front keyhole walls, leading to transient bubble formation, which is captured by the solidification front.
3) It is discovered that different keyhole pore formation mechanisms make their shapes and distributions different. The R-pore is small and unstable; thus, it is usually distributed in the upper part. RF-pore is medium-sized and nearly spherical, primarily in the middle part. The KP-pore is large and irregular, and its morphology is similar to that of the keyhole tip captured by the solidification interface. Most of the KP-pores are located at the bottom.
4) The effects of the powder on the pore formation is explored. The powder decreases the heat transfer efficiency, leading to a smaller molten pool and keyhole depth. Moreover, the presence of the powder increases the oscillation of the molten pool and keyhole, resulting in more keyhole pores.
5) The study upon the effects of input energy density uncovers that the oscillation frequency, KP-pores, and total pore counts increase with an increase in the energy density in the power function. The input-energy-density thresholds for the penetration and pore occurrence are in the following order: $E_{\text{Total pore counts}} < E_{\text{Oscillation}}$

$_{frequency} \approx E_{Maximum\ penetration\ depth} < E_{KP\text{-}pore\ counts}$. Pores are no longer be formed when the input energy density is below 0.02 MJ·cm^{-3}.

Reference

[1] L. Wang, Y. Zhang, W. Yan, Evaporation Model for Keyhole Dynamics During Additive Manufacturing of Metal, Physical Review Applied, 14 (2020).

[2] A.A. Martin, N.P. Calta, S.A. Khairallah, J. Wang, P.J. Depond, A.Y. Fong, V. Thampy, G.M. Guss, A.M. Kiss, K.H. Stone, C.J. Tassone, J. Nelson Weker, M.F. Toney, T. van Buuren, M.J. Matthews, Dynamics of pore formation during laser powder bed fusion additive manufacturing, Nat Commun, 10 (2019) 1987.

[3] C.L.A. Leung, S. Marussi, M. Towrie, J. del Val Garcia, R.C. Atwood, A.J. Bodey, J.R. Jones, P.J. Withers, P.D. Lee, Laser-matter interactions in additive manufacturing of stainless steel SS316L and 13-93 bioactive glass revealed by in situ X-ray imaging, Additive Manufacturing, 24 (2018) 647-657.

[4] C. Zhao, K. Fezzaa, R.W. Cunningham, H. Wen, F. De Carlo, L. Chen, A.D. Rollett, T. Sun, Real-time monitoring of laser powder bed fusion process using high-speed X-ray imaging and diffraction, Sci Rep, 7 (2017) 3602.

[5] M. Seifi, M. Gorelik, J. Waller, N. Hrabe, N. Shamsaei, S. Daniewicz, J.J. Lewandowski, Progress Towards Metal Additive Manufacturing Standardization to Support Qualification and Certification, Jom, 69 (2017) 439-455.

[6] M. Xia, D. Gu, G. Yu, D. Dai, H. Chen, Q. Shi, Porosity evolution and its thermodynamic mechanism of randomly packed powder-bed during selective laser melting of Inconel 718 alloy, International Journal of Machine Tools and Manufacture, 116 (2017) 96-106.

[7] M. Bisht, N. Ray, F. Verbist, S. Coeck, Correlation of selective laser melting-melt pool events with the tensile properties of Ti-6Al-4V ELI processed by laser powder bed fusion, Additive Manufacturing, 22 (2018) 302-306.

[8] H. Gong, K. Rafi, H. Gu, G.D. Janaki Ram, T. Starr, B. Stucker, Influence of defects on mechanical properties of Ti–6Al–4V components produced by selective laser melting and electron beam melting, Materials & Design, 86 (2015) 545-554.

[9] S.L.B. Kramer, T.A. Ivanoff, J.D. Madison, A.P. Lentfer, Evolution of damage and failure in an additively manufactured 316L SS structure: experimental reinvestigation of the third Sandia fracture challenge, International Journal of Fracture, 218 (2019) 63-84.

[10] J.D. Madison, O.D. Underwood, L.P. Swiler, B.L. Boyce, B.H. Jared, J.M. Rodelas, B.C. Salzbrenner, Corroborating tomographic defect metrics with mechanical response in an additively manufactured precipitation-hardened stainless steel, 2018.

[11] F.H. Kim, S.P. Moylan, Literature Review of Metal Additive Manufacturing Defects, National Institute of Standards and Technology, DOI 10.6028/nist.Ams.100-16(2018).

[12] E.W. Jost, J.C. Miers, A. Robbins, D.G. Moore, C. Saldana, Effects of spatial energy distribution-induced porosity on mechanical properties of laser powder bed fusion 316L stainless steel, Additive Manufacturing, 39 (2021).

[13] S.M.H. Hojjatzadeh, N.D. Parab, Q. Guo, M. Qu, L. Xiong, C. Zhao, L.I. Escano, K. Fezzaa, W. Everhart, T. Sun, L. Chen, Direct observation of pore formation mechanisms during LPBF additive

manufacturing process and high energy density laser welding, International Journal of Machine Tools and Manufacture, 153 (2020).
[14] A.A. Martin, N.P. Calta, J.A. Hammons, S.A. Khairallah, M.H. Nielsen, R.M. Shuttlesworth, N. Sinclair, M.J. Matthews, J.R. Jeffries, T.M. Willey, J.R.I. Lee, Ultrafast dynamics of laser-metal interactions in additive manufacturing alloys captured by in situ X-ray imaging, Materials Today Advances, 1 (2019).
[15] N.D.P. Cang Zhao, Xuxiao Li, Kamel Fezzaa, Wenda Tan, Anthony D. Rollett, Tao Sun, Critical instability at moving keyhole tip generates porosity in laser melting, Science, 370 (2020) 1080-1086.
[16] M. Miyagi, H. Wang, R. Yoshida, Y. Kawahito, H. Kawakami, T. Shoubu, Effect of alloy element on weld pool dynamics in laser welding of aluminum alloys, Sci Rep, 8 (2018) 12944.
[17] Q. Guo, M. Qu, L.I. Escano, S.M.H. Hojjatzadeh, Z. Young, K. Fezzaa, L. Chen, Revealing melt flow instabilities in laser powder bed fusion additive manufacturing of aluminum alloy via in-situ high-speed X-ray imaging, International Journal of Machine Tools and Manufacture, DOI 10.1016/j.ijmachtools.2022.103861(2022).
[18] Y. Huang, T.G. Fleming, S.J. Clark, S. Marussi, K. Fezzaa, J. Thiyagalingam, C.L.A. Leung, P.D. Lee, Keyhole fluctuation and pore formation mechanisms during laser powder bed fusion additive manufacturing, Nat Commun, 13 (2022) 1170.
[19] R. Wang, D. Gu, K. Lin, C. Chen, Q. Ge, D. Li, Multi-material additive manufacturing of a bio-inspired layered ceramic/metal structure: Formation mechanisms and mechanical properties, International Journal of Machine Tools and Manufacture, 175 (2022).
[20] C. Tang, K.Q. Le, C.H. Wong, Physics of humping formation in laser powder bed fusion, International Journal of Heat and Mass Transfer, 149 (2020).
[21] D. Wu, X. Hua, F. Li, L. Huang, Understanding of spatter formation in fiber laser welding of 5083 aluminum alloy, International Journal of Heat and Mass Transfer, 113 (2017) 730-740.
[22] L. Li, G. Peng, J. Wang, J. Gong, S. Meng, Numerical and experimental study on keyhole and melt flow dynamics during laser welding of aluminium alloys under subatmospheric pressures, International Journal of Heat and Mass Transfer, 133 (2019) 812-826.
[23] D. Gu, M. Xia, D. Dai, On the role of powder flow behavior in fluid thermodynamics and laser processability of Ni-based composites by selective laser melting, International Journal of Machine Tools and Manufacture, 137 (2019) 67-78.
[24] X. Li, Q. Guo, L. Chen, W. Tan, Quantitative investigation of gas flow, powder-gas interaction, and powder behavior under different ambient pressure levels in laser powder bed fusion, International Journal of Machine Tools and Manufacture, 170 (2021).
[25] A. Charles, M. Bayat, A. Elkaseer, L. Thijs, J.H. Hattel, S. Scholz, Elucidation of dross formation in laser powder bed fusion at down-facing surfaces: Phenomenon-oriented multiphysics simulation and experimental validation, Additive Manufacturing, 50 (2022).
[26] C. Panwisawas, B. Perumal, R.M. Ward, N. Turner, R.P. Turner, J.W. Brooks, H.C. Basoalto, Keyhole formation and thermal fluid flow-induced porosity during laser fusion welding in titanium alloys: Experimental and modelling, Acta Materialia, 126 (2017) 251-263.
[27] S.A. Khairallah, T. Sun, B.J. Simonds, Onset of periodic oscillations as a precursor of a transition to pore-generating turbulence in laser melting, Additive Manufacturing Letters, 1 (2021).
[28] M. Bayat, A. Thanki, S. Mohanty, A. Witvrouw, S. Yang, J. Thorborg, N.S. Tiedje, J.H. Hattel, Keyhole-induced porosities in Laser-based Powder Bed Fusion (L-PBF) of Ti6Al4V: High-fidelity

modelling and experimental validation, Additive Manufacturing, 30 (2019).
[29] M. Bayat, S. Mohanty, J.H. Hattel, Multiphysics modelling of lack-of-fusion voids formation and evolution in IN718 made by multi-track/multi-layer L-PBF, International Journal of Heat and Mass Transfer, 139 (2019) 95-114.
[30] L. Wang, Y. Zhang, H.Y. Chia, W. Yan, Mechanism of keyhole pore formation in metal additive manufacturing, npj Computational Materials, 8 (2022).
[31] D. Wu, X. Hua, L. Huang, F. Li, Y. Cai, Elucidation of keyhole induced bubble formation mechanism in fiber laser welding of low carbon steel, International Journal of Heat and Mass Transfer, 127 (2018) 1077-1086.
[32] Y.H. Chen, S.J. Clark, C.L.A. Leung, L. Sinclair, S. Marussi, M.P. Olbinado, E. Boller, A. Rack, I. Todd, P.D. Lee, In-situ Synchrotron imaging of keyhole mode multi-layer laser powder bed fusion additive manufacturing, Applied Materials Today, 20 (2020).
[33] H. Yang, J. Wu, Q. Wei, Z. Tang, A. Wang, X. Jin, X. Li, Y. Wu, G. Lu, H. Wang, H. Wang, Stable cladding of high reflectivity pure copper on the aluminum alloy substrate by an infrared-blue hybrid laser, Additive Manufacturing Letters, 3 (2022).
[34] J. Liu, P. Wen, Metal vaporization and its influence during laser powder bed fusion process, Materials & Design, 215 (2022).
[35] J. Ye, S.A. Khairallah, A.M. Rubenchik, M.F. Crumb, G. Guss, J. Belak, M.J. Matthews, Energy Coupling Mechanisms and Scaling Behavior Associated with Laser Powder Bed Fusion Additive Manufacturing, Advanced Engineering Materials, 21 (2019).
[36] Q.W. Liping Guo, Hongze Wang, Hanjie Liu, A comprehensive model to quantify the effects of additional nano-particles on the printability in laser powder bed fusion of aluminum alloy and composite, Additive Manufacturing, 58 (2022) 103011.
[37] M.A.B. Cook P Simulation of melt pool behaviour during additive manufacturing: Underlying physics and progress, Additive Manufacturing, 31 (2020).
[38] K. Hirano, R. Fabbro, M. Muller, Experimental determination of temperature threshold for melt surface deformation during laser interaction on iron at atmospheric pressure, Journal of Physics D: Applied Physics, 44 (2011).
[39] S. Pang, K. Hirano, R. Fabbro, T. Jiang, Explanation of penetration depth variation during laser welding under variable ambient pressure, Journal of Laser Applications, 27 (2015).
[40] H. Wang, Y. Zou, Microscale interaction between laser and metal powder in powder-bed additive manufacturing: Conduction mode versus keyhole mode, International Journal of Heat and Mass Transfer, 142 (2019).
[41] R. Lin, H.-p. Wang, F. Lu, J. Solomon, B.E. Carlson, Numerical study of keyhole dynamics and keyhole-induced porosity formation in remote laser welding of Al alloys, International Journal of Heat and Mass Transfer, 108 (2017) 244-256.
[42] Y.M. Wang, T. Voisin, J.T. McKeown, J. Ye, N.P. Calta, Z. Li, Z. Zeng, Y. Zhang, W. Chen, T.T. Roehling, R.T. Ott, M.K. Santala, Philip J. Depond, M.J. Matthews, A.V. Hamza, T. Zhu, Additively manufactured hierarchical stainless steels with high strength and ductility, Nature Materials, 17 (2017) 63-71.
[43] C.Z. Ross Cunningham, Niranjan Parab, Christopher Kantzos, Joseph Pauza, Kamel Fezzaa, Tao Sun, Anthony D. Rollett, Keyhole threshold and morphology in laser melting revealed by ultrahigh-speed x-ray imaging, Science, 363 (2019) 849–852.
[44] A. Bobel, L.G. Hector, I. Chelladurai, A.K. Sachdev, T. Brown, W.A. Poling, R. Kubic, B. Gould, C.

Zhao, N. Parab, A. Greco, T. Sun, In situ synchrotron X-ray imaging of 4140 steel laser powder bed fusion, Materialia, 6 (2019).
[45] I. Bitharas, N. Parab, C. Zhao, T. Sun, A.D. Rollett, A.J. Moore, The interplay between vapour, liquid, and solid phases in laser powder bed fusion, Nat Commun, 13 (2022) 2959.